



High-resolution clustered pinhole ^{131}I Iodine SPECT imaging in mice

Frans van der Have ^{a,b,c}, Oleksandra Ivashchenko ^{a,b,c,*}, Marlies C. Goorden ^a,
Ruud M. Ramakers ^{a,b,c}, Freek J. Beekman ^{a,b,c}

^a Section Radiation, Detection and Medical Imaging, Delft University of Technology, Mekelweg 15, 2629 JB, Delft, The Netherlands

^b MIlabs B.V., Heidelberglaan 100 STR 4.105, 3584, CX, Utrecht, The Netherlands

^c Department for Translational Neuroscience, Brain Center Rudolf Magnus, University Medical Center Utrecht, 3584, CG, Utrecht, The Netherlands

ARTICLE INFO

Article history:

Received 5 April 2016

Received in revised form 12 May 2016

Accepted 28 May 2016

Keywords:

SPECT

Molecular imaging

Radioiodine

Radioimmunotherapy

ABSTRACT

Introduction: High-resolution pre-clinical ^{131}I SPECT can facilitate development of new radioiodine therapies for cancer. To this end, it is important to limit resolution-degrading effects of pinhole edge penetration by the high-energy γ -photons of iodine. Here we introduce, optimize and validate ^{131}I SPECT performed with a dedicated high-energy clustered multi-pin-hole collimator.

Methods: A SPECT–CT system (VECTor/CT) with stationary gamma-detectors was equipped with a tungsten collimator with clustered pinholes. Images were reconstructed with pixel-based OSEM, using a dedicated ^{131}I system matrix that models the distance- and energy-dependent resolution and sensitivity of each pinhole, as well as the intrinsic detector blurring and variable depth of interaction in the detector. The system performance was characterized with phantoms and *in vivo* static and dynamic ^{131}I -NaI scans of mice.

Results: Reconstructed image resolution reached 0.6 mm, while quantitative accuracy measured with a ^{131}I filled syringe reaches an accuracy of $+3.6 \pm 3.5\%$ of the gold standard value. *In vivo* mice scans illustrated a clear shape of the thyroid and biodistribution of ^{131}I within the animal. Pharmacokinetics of ^{131}I was assessed with 15-s time frames from the sequence of dynamic images and time–activity curves of ^{131}I -NaI.

Conclusions: High-resolution quantitative and fast dynamic ^{131}I SPECT in mice is possible by means of a high-energy collimator and optimized system modeling. This enables analysis of ^{131}I uptake even within small organs in mice, which can be highly valuable for development and optimization of targeted cancer therapies.

© 2016 Elsevier Inc. All rights reserved.

1. Introduction

Although the combined γ - and β -emitter ^{131}I is best known for its use in thyroid cancer therapy, it is also an important nuclide for other existing and new therapeutic approaches. As an example, ^{131}I has been used in treating non-Hodgkin's [1–4] and Hodgkin's lymphoma [5], also liver cancer [6,7]. Alkylphosphocholine analogs labeled with ^{131}I were reported to be very promising for therapy of a broad spectrum of solid tumors [8]. Furthermore, the use of sodium–iodine symporter (NIS) mediated uptake of ^{131}I , following transfection of NIS-containing vectors into non-NIS-bearing tissues, recently showed successful results in antibody-based treatment of non-Hodgkin's lymphoma [9], gene transfer [10,11], and viral and cell-based [12,13] therapeutic approaches for cancer. Nevertheless, despite the standard use of direct ^{131}I SPECT imaging in the clinic (*i.e.* for monitoring the response to therapy and patient-specific dose calculations), low resolution and poor quantification accuracy of *in vivo* ^{131}I imaging in the pre-clinical field [14] requires *ex vivo* analyses [8,13] or the use of imaging substitutes ($^{99\text{m}}\text{Tc}$ -pertechnetate or $^{123}\text{I}/^{124}\text{I}$ -based compounds) [15] for the

assessment of therapy progression. If it were available, quantitative and high-resolution SPECT imaging of ^{131}I in small animals would benefit the development of translational radioisotope therapies.

Imaging ^{131}I in mice is rather challenging due to the relatively high energy of its gamma photons (364 keV), that consequently penetrate the collimator wall and pinhole edges. Although extensive investigations on optimal collimator design [16,17] and system modeling [18–20] for medium- to high-energy clinical SPECT were performed, pre-clinical ^{131}I imaging with sub-mm resolution was not possible up to now. Recently, SPECT and PET imaging have been combined in a novel versatile emission computed tomography system (VECTor, MIlabs, The Netherlands) [21] that showed simultaneous sub-mm imaging of $^{99\text{m}}\text{Tc}$ and ^{18}F by means of a dedicated clustered multi-pin-hole (CMP) collimator. Compared to pinholes used in conventional SPECT collimators, the pinholes in the CMP collimator have narrower opening angles (Fig. 1,a), which significantly decreases the penetration of the photons through the pinhole edges. Due to VECTor's ability to deal with high energy annihilation photons, it is interesting to investigate its ability to image the 364 keV photons from ^{131}I .

The aim of this study is to optimize and characterize VECTor for performing *in vivo* ^{131}I mouse SPECT imaging. To this end, we first optimized image reconstruction for imaging 364 keV photons of ^{131}I

* Corresponding author. Tel.: +31 0 621396112.

E-mail address: O.Ivashchenko-1@tudelft.nl (O. Ivashchenko).

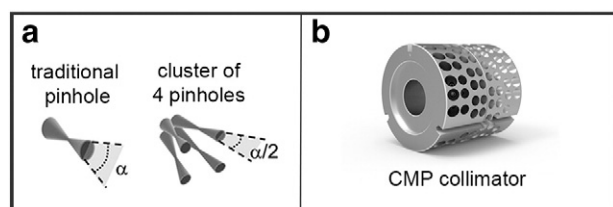


Fig. 1. (a) Traditional pinhole with opening angle α and cluster of 4 pinholes with approximately the same field of view and opening angle $\alpha/2$. (b) CMP collimator optimized for imaging high energy gamma rays.

and evaluated the quantification accuracy and image quality of ^{131}I SPECT using multiple phantoms. Additionally, we show several examples of *in vivo* imaging performance with multiple static and dynamic ^{131}I -sodium iodide (NaI) SPECT/CT scans of mice.

2. Materials and methods

2.1. Imaging system

The detector geometry and scanner design of VECTor are equivalent to those of the U-SPECT system (MILabs B.V., The Netherlands) [22]. The VECTor system uses a CMP collimator (Fig. 1,b) mounted in the center of three large NaI(Tl) gamma cameras in a triangular setup. The CMP collimator used for this study consists of a tungsten cylinder with a wall thickness of 43 mm and it enables collimating gamma photons up to approximately 600 keV. The collimator contains 162 0.7-mm-diameter pinholes, organized in clusters of 4 pinholes (Fig. 1,a). The pinholes in the inner 2 rings of the collimator have opening angles of 18° , while the outer rings contain 16° opening angle pinholes. More details about the geometry of the collimator can be found in Goorden et al. [21]. All the pinhole clusters together observe a field of view that extends over the entire collimator tube diameter [23]. The part of the field of view (CFOV) that is seen by all clusters simultaneously, the so called “central field of view” (an ellipsoid of $12 \times 12 \times 7$ mm), provides complete data sampling (sufficient angular data to reconstruct an image) without any translations of the animal bed. Note that such an area does not exist in traditional systems, since they require rotation of heavy gamma ray detectors to get sufficient angular data. Complete data (up to total body mouse imaging) are obtained by moving the animal through the scanner in a multi-planar or spiral trajectory [24]. Data are collected in list-mode.

2.2. Image reconstruction and analyzing

The activity distributions were reconstructed from the list-mode data using pixel-based OSEM [25] with resolution recovery and compensation for distance-dependent pinhole sensitivity. The system matrix was calculated in three different ways in order to be able to compare the reconstructed images based on the same acquired data. The first model was based on $^{99\text{m}}\text{Tc}$ point source measurements [26], resulting in a system matrix suitable for reconstructing $^{99\text{m}}\text{Tc}$ (140 keV) and other low-energy isotopes. The second model was the model that is normally used in VECTor for reconstructing positron emitters such as ^{18}F (511 keV). The position and orientation of the collimators and detectors were determined by means of a geometrical fit from the $^{99\text{m}}\text{Tc}$ point source measurements [26]. Given the energy-specific values of the linear attenuation coefficients of the collimator (modeling edge penetration) and detector (modeling depth of interaction) materials, the system matrix was calculated by an analytical ray-tracing code as described in Goorden et al. [27–28]. The third model used the same ray-tracing code as the second, where the linear attenuation coefficients for the collimator and detector were set for 364 keV, resulting in a dedicated system matrix for reconstructing ^{131}I .

For the SPECT images shown, we reconstructed images for 50 iterations and 32 subsets [25] with an isotropic 0.25 mm voxel grid. A 20% ^{131}I photo peak window centered at 364 keV was used. Two background windows were placed on both sides of the photo peak window with a width of 4% of the photo peak energy, i.e. 14.2 keV each. Compton scatter correction was applied via the triple energy-window method [29]. All SPECT images were attenuation corrected using CT data [30]. After this, absolute quantification of the images was enabled using a scaling factor obtained from scanning a small ^{131}I source with known activity [30].

Image volumes used for time-activity curve (TAC) generation were reconstructed as a dynamic frame sequence, decay-corrected, but otherwise unprocessed. TACs were generated for two ROIs that were manually drawn around the left lobe of the thyroid and salivary gland. The uptake in the ROI was calculated as the percentage injected dose per mL of tissue volume (%ID/mL).

For visual representation in the manuscript, reconstructed volumes of SPECT scans were post filtered with a 0.35 mm FWHM 3D Gaussian filter.

2.3. Phantom experiments

The peak sensitivity of the collimator was measured in counts per second per MBq of activity (cps/MBq) by scanning a small ^{131}I source of known activity placed in the center of the “central field of view”.

The spatial resolution was determined with micro-hot-rod capillary resolution phantom scans. The phantom consists of 6 sectors with rods of 1.0, 0.8, 0.7, 0.6, 0.5 and 0.4 mm diameter. The minimal distance between the capillaries in each sector equals the capillary diameter in that sector. The phantom was filled with 76 MBq of ^{131}I -NaI solution. A two-hour SPECT scan with 30-min time frames was performed.

The quantification accuracy of reconstructed images was evaluated by means of scanning a 20 mL syringe (19 mm diameter) that was filled up to 6.5 mL with 12.69 MBq/mL ^{131}I -NaI and scanned for 2 h. The activity in the syringe was measured in a dose calibrator (VDC-304, Veenstra Instruments, The Netherlands) with an accuracy of $\pm 3\%$ or ± 0.38 MBq/mL.

2.4. In vivo animal experiments

Animal experiments were performed with healthy C57Bl/6 mice according to protocols approved by the Animal Ethical Committee of the UMC Utrecht and in accordance with Dutch Law on Animal Experimentation.

Two mice were anesthetized with isoflurane and injected with respectively 60 (mouse 1) and 5 MBq (mouse 2) ^{131}I -NaI via the tail vein. Fifteen minutes after the injection, 15-min total body SPECT scans followed by 15-min focused thyroid scans were performed on each animal. After the end of the SPECT acquisition total body X-ray CT scans were acquired.

One mouse was anesthetized with isoflurane and a tail vein catheter pre-filled with saline was placed. Just after the start of a dynamic 30-min focused thyroid SPECT scan the animal was injected with 26 MBq of ^{131}I -NaI. The first 15 min of the scan was acquired using 15-s time frames, for the remainder the frame duration was increased to one minute.

3. Results

3.1. Phantom scans

In this section we evaluate the ^{131}I imaging performance of VECTor based on resolution and uniformity phantom scans reconstructed with three types of system matrixes: one containing a dedicated system model for ^{131}I (364 keV) and two standard models used in VECTor, one for $^{99\text{m}}\text{Tc}$ (140 keV) and one for ^{18}F (511 keV) photons. This was done to assess the level of improvement in VECTor's performance for quantitative ^{131}I imaging.

Fig. 2 shows a 4-mm-thick slice from the resolution phantom scan with ^{131}I . The reconstructed image resolution was evaluated for 120

and 30 min image acquisition. With the dedicated 364 keV modeling the best resolution was obtained for 120 min acquisition reconstruction: the minimal visible rods have 0.5 mm diameter. A decrease in acquisition time to 30 min, results in some resolution loss, yet all rods from the 0.6 mm segment can still be clearly distinguished. With the ^{99m}Tc model incorporated in the matrix 0.7 mm resolution is reached for both acquisition times, but there is a much stronger background and the shape of the largest round rods appears triangulated. This is probably caused by the mismatch of the depth of interaction in the crystal between 140 and 364 keV. The ^{18}F model for image reconstruction results in the worst resolution out of three models (>0.7 mm), yet shows only minor shape distortions of the rods. In this case the dominant inaccuracy in the modeling is probably the higher pinhole edge penetration at 511 keV that is assumed in the model. Even though the use of ^{18}F modeling for reconstructions of *in vivo* animal scans will not cause strong shape distortion of anatomical structures, essentially important spatial resolution will be noticeably degraded compared to dedicated ^{131}I modeling.

Fig. 3 shows the results from a uniform filled syringe scan, reconstructed by the same three system models as used in Fig. 2. The syringe scan was used to assess the quantification accuracy of ^{131}I SPECT. From the volumes, 2 mm wide line profiles were extracted. The activity concentration of ^{131}I based on the measurement in the dose calibrator (“gold standard”) is indicated with an orange line on the profile plots. The average activity concentrations in the syringe calculated from the reconstructed image volumes [30] were 13.15 ± 0.43 MBq/mL (^{131}I modeling, black), 11.59 ± 0.88 MBq/mL (^{99m}Tc modeling, green) and 13.32 ± 0.40 MBq/mL (^{18}F modeling, red). Relative to the gold standard value, this is respectively $+3.6 \pm 3.5\%$, $-8.5 \pm 7\%$ and $+5 \pm 3.2\%$. The peak sensitivity for ^{131}I at the center of the collimator, measured with a small ^{131}I source, was determined to be 1578 cps/MBq or 0.16%.

Based on quantification accuracy and image resolution achieved with the three system models compared in this work, the dedicated ^{131}I model

showed to be the most suitable for applications in quantitative and high-resolution small-animal SPECT imaging.

3.2. In vivo animal scans

In this section we illustrate the *in vivo* imaging performance of VEC-Tor with the dedicated system modeling for ^{131}I SPECT based on static and dynamic ^{131}I -NaI SPECT/CT scans of mice.

Fig. 4 shows axial and coronal slices (1 mm thick) through the mouse thyroids from the focused scans with 60 MBq (mouse 1) and 5 MBq (mouse 2) of ^{131}I -NaI. For both levels of activity the two lobes of the glands are well separated on the images and the anatomical shape of the glands is as expected [31]. Although the level of injected activity was decreased by a factor of 12 (from 60 to 5 MBq), the maximal activity concentration on the slices of the thyroid decreased by only a factor of 3.2 (from 171 MBq/mL to 54 MBq/mL). Considering that we used i.v. administration of the tracer [32] and the fact that there is at least 222 GBq/mg iodine in the ^{131}I -NaI solution at the time of radiolabeling (information provided by GE Healthcare), the amount of iodide that was administered to mouse 1 (60 MBq) could have approached the recommended thyroid-blocking concentration of iodide for mice [33]. Thus, such a difference in ^{131}I -NaI concentrations in thyroids of the two animals (Figs. 4 and 5) might be related to saturation of possible binding sites in the glands at the higher level of activity concentration (60 MBq) [33–35]. Complete understanding of this effect requires further investigations that lie outside the scope of this paper.

Maximum intensity projections (MIPs) of the total body scans (Fig. 5) illustrate the ^{131}I -NaI biodistribution for the corresponding focused acquisitions. As expected, the tracer is seen to primarily accumulate in the stomach and thyroid.

Fig. 6,a shows a set images of individual 15-s time frames (1 mm slices, mouse 3) that illustrates the ability to assess kinetics of the ^{131}I -NaI uptake in the thyroid. At the same time, quantitative dynamics of the uptake can be further investigated on the TACs (Fig. 6,b). Due to high correlation between the uptake dynamics in the lobes of the thyroid, it was decided not to include the right lobe in the TACs graph to simplify the visual representation of the data, but the graph containing TACs from both lobes of the thyroid is available in the supporting information (Fig. S1).

It is clear from the set of dynamic images (Fig. 6,a) that the accumulation of ^{131}I -NaI in the thyroid is rapid and starts from 30 s post injection onwards. Such results agree with both the expected biodynamics of NaI [35] and the dynamics of the tracer in the left lobe of the glands on the TACs (Fig. 6,b), indicating that the ^{131}I -NaI concentration rapidly increases in the first 10 min post injection and retains a slow rate of increase for the remaining time of the scan.

4. Discussion

The use of ^{131}I for targeted radiotherapies of cancer is already widely applied in treatment of iodine-specific tumors [6] and novel approaches that are being developed today seem to have a high potential to treat a broad spectrum of tumor types [8,10,11]. At the same time, pre-clinical *in vivo* research using ^{131}I is rather difficult, due to poor image quality and limited resolution of ^{131}I SPECT [14]. Therefore, the majority of pre-clinical ^{131}I therapies require extensive *ex vivo* analyzing [8]. The phantom experiments in this work showed that with optimized system modeling and a dedicated high-energy collimator high-resolution quantitative imaging of ^{131}I becomes possible with a pre-clinical SPECT system, despite the relatively high energy of the emitted γ -photons.

In small-animal imaging, reconstructed image resolution plays an important role as it allows to distinguish between different organs that can accumulate iodine and might lie in relative proximity to each other (e.g. the thyroid and salivary gland). At the same time, a high resolution allows to minimize partial-volume-effect-related errors in

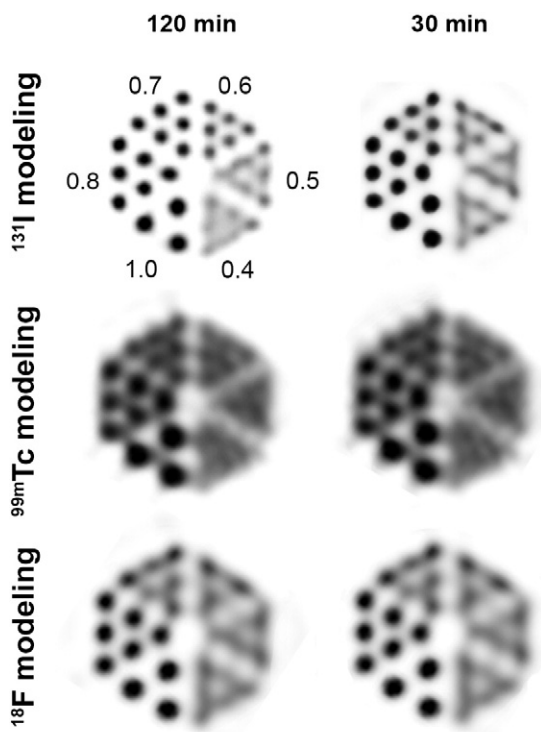


Fig. 2. Slices from the reconstructed image of the hot-rod resolution phantom with 76 MBq ^{131}I . Three ways of modeling the system were used in image reconstruction: dedicated ^{131}I modeling and two standard system models of the VEC-Tor, ^{99m}Tc and ^{18}F modeling.

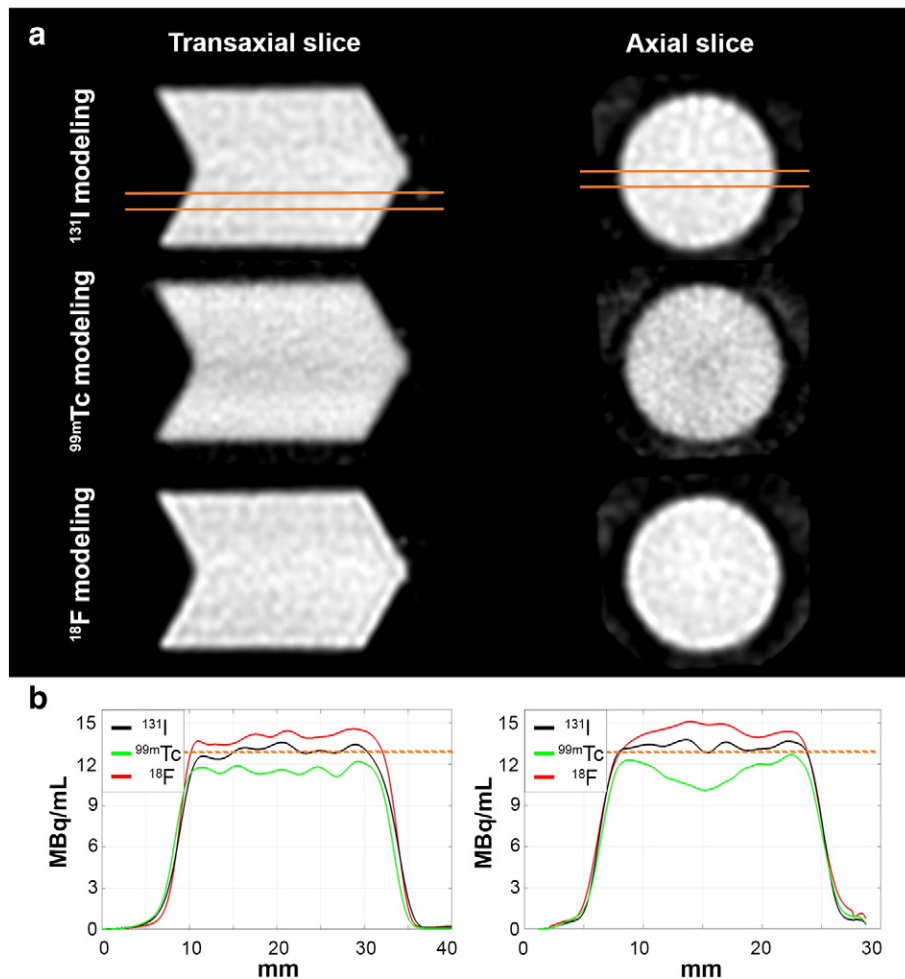


Fig. 3. (a) Axial and transaxial slices through the ^{131}I uniformly filled syringe, reconstructed with three different system models (^{131}I , $^{99\text{m}}\text{Tc}$ and ^{18}F modeling) and compared at equal resolution. (b) Line profiles through the phantom, drawn as indicated on the slices' images. The activity concentration measured in the dose calibrator is indicated with orange lines on the line profile plots.

quantification of SPECT images [36]. The resolution phantom scan in the paper illustrates that sub-mm resolution ^{131}I SPECT can be performed by means of dedicated ^{131}I system modeling and use of a high-energy clustered pinhole collimator. Furthermore, a high quantification accuracy ($+3.6 \pm 3.5\%$ from the “gold standard”, Fig. 3,b) of SPECT scans was found. Such performance of VECTOR not only improves current ^{131}I

SPECT image quality [14] for the assessment of compounds' biodistributions, but also provides an opportunity to perform quantitative analysis of the uptake, and based on that to calculate animal-specific *in vivo* 3D dose distribution [37].

The results of the *in vivo* animal evaluation using ^{131}I -Nal illustrated that it is possible to image small anatomical structures with high level of details (e.g. a clear shape and separation between the lobes of the thyroid) already in total body acquisitions (Fig. 5).

Tracer pharmacokinetics provides the link between the distribution of radioactivity in the tissue over time and relevant physiological parameters or disease state, particularly during development of new therapeutic approaches. Thus, dynamic imaging capabilities were further assessed with a dynamic ^{131}I -Nal scan of the mouse thyroid using 15-s time frames. We showed that it is possible to assess tracer dynamics in the thyroid and salivary glands not just from the time-activity curves (Fig. 6,b), but also from the dynamic sequence of SPECT images (Fig. 6,a), illustrating the biodistribution of the radiolabeled compound within the organ or system of organs. We expect that this capability can be translated to other applications of ^{131}I imaging for e.g. dynamic analysis of intra-tumoral accumulation of ^{131}I -labeled compounds. At the same time, because most organs are larger than the thyroid, the visible level of detail relative to the organ size can be effectively higher.

Radioactive iodine, unlike other NIS substrates, can be oxidized and bound to proteins and lipids [38]. Therefore, the uptake of other iodine- or NIS-based imaging substitutes that might be used for imaging of response to ^{131}I therapy will be partially inhibited by already present

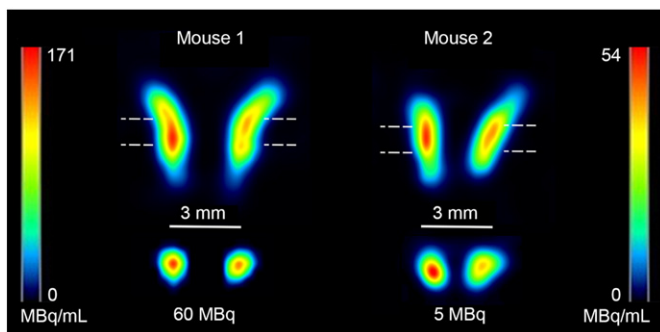


Fig. 4. *In vivo* imaging performance of ^{131}I SPECT with VECTOR. Images show coronal and axial slices from focused 60 MBq (mouse 1) and 5 MBq (mouse 2) ^{131}I -Nal thyroid scans of two animals. These images clearly illustrate the biodistribution of the tracer within the lobes and show the detailed anatomical structure of the lobes as well. Dashed white lines on the coronal view indicate position of axial view slices.

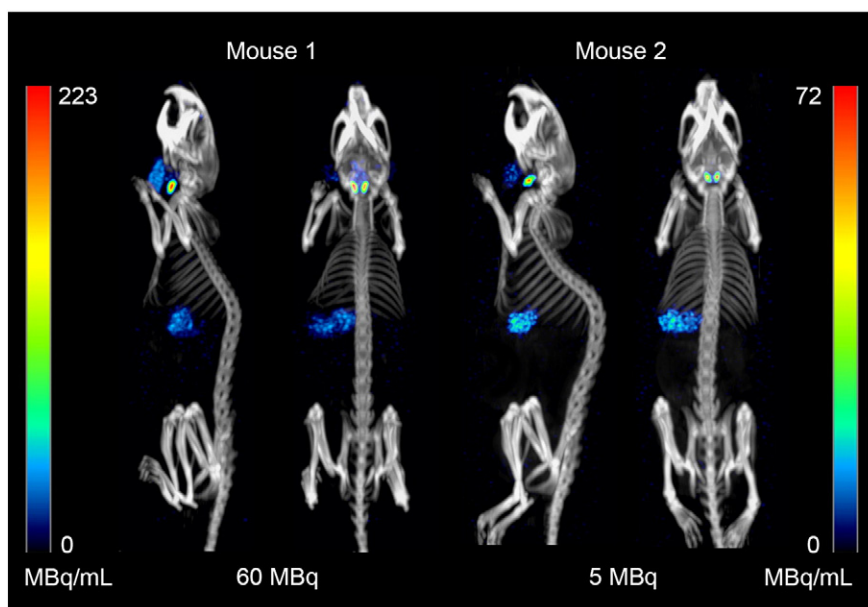


Fig. 5. MIPs of total body mouse SPECT/CT scans with 60 MBq (mouse 1) and 5 MBq (mouse 2) of ^{131}I -NaI show accumulation of the compound in the stomach, thyroid and in the salivary glands.

iodine in the animal body [39]. As a result, their biodistribution may not be directly proportional to that of the therapeutic ^{131}I compound (or the other way around). With the currently obtained imaging performance for ^{131}I , we expect that it is possible to directly monitor response to therapy in mice with ^{131}I SPECT, instead of having to rely on $^{99\text{m}}\text{Tc}$ -pertechnetate, ^{124}I or ^{123}I as a substitute [10,8,13]. Additionally, not requiring an additional imaging agent during monitoring of ^{131}I therapy will decrease the total cost and complexity of the study.

5. Conclusion

We have shown that it is possible to quantitatively image ^{131}I and reach resolution below 0.6 mm. This was performed with a SPECT-CT system equipped with a dedicated high-energy collimator. Employing dedicated energy-specific system modeling is very advantageous for obtaining optimal image quality. Dynamic *in vivo* ^{131}I -NaI SPECT imaging capabilities were illustrated in a mouse as well.

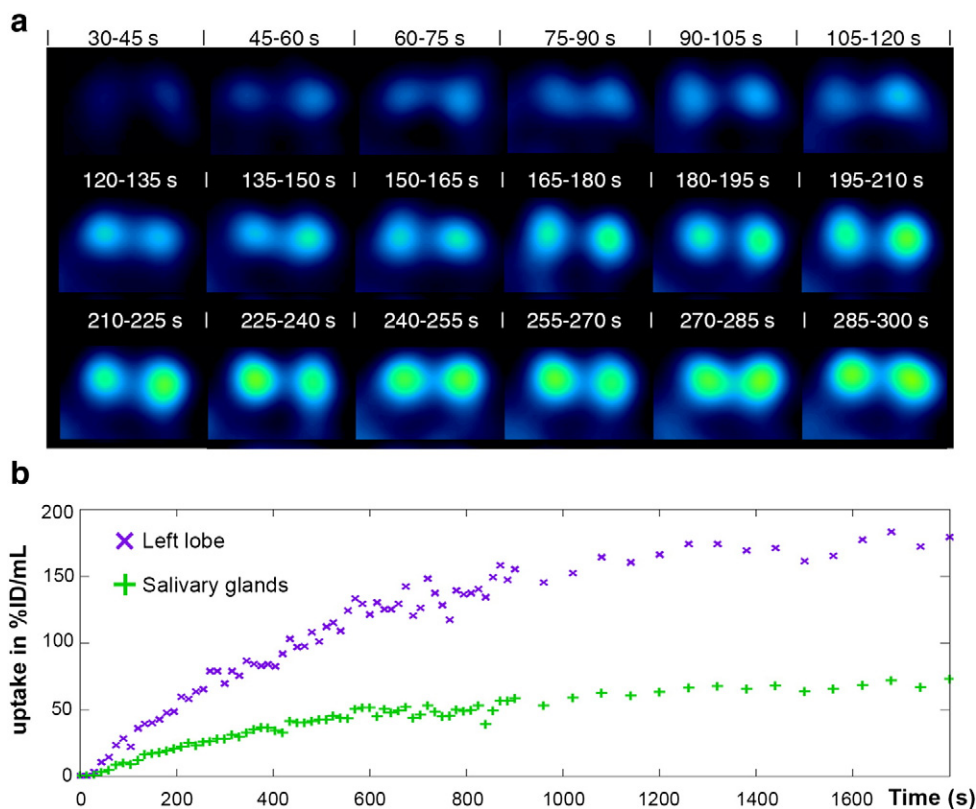


Fig. 6. Axial slices through mouse thyroid (a) illustrate early stage dynamics of ^{131}I -NaI uptake in the mouse, obtained from focused dynamic 26 MBq Na^{131}I thyroid SPECT scan with 15-s time frames and ^{131}I modeling in the system matrix. (b) Time-activity curves of ^{131}I -NaI uptake by left lobe of the thyroid and salivary glands.

Conflict of interest

Freek J. Beekman is a founder, shareholder and CEO of MILabs. Frans van der Have is a shareholder of MILabs.

Ethical approval

All applicable institutional and/or national guidelines for the care and use of animals were followed.

Funding

The research leading to these results has received funding from the People Program (Marie Curie Actions) of the European Union's Seventh Framework Program (FP7/2007–2013) under REA grant agreement no. PITN-GA-2012-317019 'TRACE 'n TREAT'.

Supplementary Materials

Supplementary data to this article can be found online at <http://dx.doi.org/10.1016/j.nucmedbio.2016.05.015>.

References

- [1] Kaminski MS, Tuck M, Estes J, et al. I-131-tositumomab therapy as initial treatment for follicular lymphoma. *N Engl J Med* 2005;352(5):441–9.
- [2] Kaminski MS, Zelenetz AD, Press OW, et al. Pivotal study of iodine I-131 Tositumomab for chemotherapy-refractory low-grade or transformed low-grade B-cell non-Hodgkin's lymphomas. *J Clin Oncol* 2001;19(19):3918–28.
- [3] Kaminski MS, Estes J, Zasadny KR, et al. Radioimmunotherapy with iodine I-131 tositumomab for relapsed or refractory B-cell non-Hodgkin lymphoma: updated results and long-term follow-up of the University of Michigan experience. *Blood* 2000;96(4):1259–66.
- [4] Gopal AK, Rajendran JG, Gooley TA, et al. High-Dose [131I]Tositumomab (anti-CD20) Radioimmunotherapy and Autologous Hematopoietic Stem-Cell Transplantation for Adults ≥ 60 Years Old With Relapsed or Refractory B-Cell Lymphoma. *J Clin Oncol* 2007;25(11):1396–402.
- [5] Sauer S, Erba PA, Petrini M, et al. Expression of the oncofetal ED-B-containing fibronectin isoform in hematologic tumors enables ED-B-targeted 131I-L19SIP radioimmunotherapy in Hodgkin lymphoma patients. *Blood* 2009;113(10):2265–74.
- [6] Chen ZN, Mi L, Xu J, et al. Targeting radioimmunotherapy of hepatocellular carcinoma with iodine (131I) metuximab injection: clinical phase I/II trials. *Int J Radiat Oncol Biol Phys* 2006;65(2):435–44.
- [7] Ychou M, Ricard M, Lumbroso J, et al. Potential contribution of 131I-labelled monoclonal anti-CEA antibodies in the treatment of liver metastases from colorectal carcinomas: pretherapeutic study with dose recovery in resected tissues. *Eur J Cancer* 1993;29A(8):1105–11.
- [8] Weichert JP, Clark PA, Kandela IK, et al. Alkylphosphocholine Analogs for Broad-Spectrum Cancer Imaging and Therapy. *Sci Transl Med* 2014;6(240):240ra75.
- [9] Cheson BD, Leonard JP. Monoclonal Antibody Therapy for B-Cell Non-Hodgkin's Lymphoma. *N Engl J Med* 2008;359:613–26.
- [10] Marsee DK, Shen DH, MacDonald LR, et al. Imaging of metastatic pulmonary tumors following NIS gene transfer using single photon emission computer tomography. *Cancer Gene Ther* 2004;11:121–7.
- [11] Mitrofanova E, Unfer R, Vahanian N, et al. Effective Growth Arrest of Human Colon Cancer in Mice Using Rat Sodium Iodide Symporter and Radioiodine Therapy. *Hum Gene Ther* 2005;16(11):1333–7.
- [12] Penheiter AR, Russel SJ, Carlson SK. The Sodium Iodide Symporter (NIS) as an Imaging Reporter for Gene, Viral, and Cell-based Therapies. *Curr Gene Ther* 2012;12(1):33–47.
- [13] Miest TS, Frenke M, Cattaneo R. Measles Virus Entry Through the Signalling Lymphocyte Activation Molecule Governs Efficacy of Mantle Cell Lymphoma Radiotherapy. *Mol Ther* 2013;21(11):2019–31.
- [14] Fan Q, Cai H, Yang H, et al. Biological Evaluation of 131I- and CF750-Labeled Dmab(scFv)-Fc Antibodies for Xenograft Imaging of CD25-Positive Tumors. *BioMed Res Int* 2014. <http://dx.doi.org/10.1155/2014/459676>.
- [15] Schipper ML, Riese CG, Seitz S, et al. Efficacy of ^{99m}Tc pertechnetate and ¹³¹I radioisotope therapy in sodium/iodide symporter (NIS)-expressing neuroendocrine tumors expressing neuroendocrine tumors in vivo. *Eur J Nucl Med Mol Imaging* 2007;34:638–50.
- [16] Tenney CR, Smith MF, Greer KL, Jaszczak RJ. Uranium Pinhole Collimators for I-131 SPECT Imaging. *IEEE Trans Nucl Sci* 1999;46(4):1165–71.
- [17] Smith MF, Jaszczak RJ, Wang H, Li J. Lead and Tungsten Pinhole Inserts for I-131 SPECT Tumor Imaging: Experimental Measurements and Photon Transport Simulations. *IEEE Trans Nucl Sci* 1997;44(1):74–82.
- [18] Dewaraja YK, Liungberg M, Koral KF. Characterization of Scatter and Penetration Using Monte Carlo Simulation ¹³¹I Imaging. *J Nucl Med* 2000;41(1):123–30.
- [19] Rault E, Vandenberghe S, Van Holen R, et al. Comparison of Image Quality of Different Iodine Isotopes (I-123, I-124, and I-131). *Cancer Biother Radiopharm* 2007;22(3):423–30.
- [20] Van Holen R, Staelens S, Vandenberghe S. SPECT imaging of high isotopes and isotopes with high energy contaminants with rotating slit collimators. *Med Phys* 2009;36:4257–67.
- [21] Goorden MC, van der Have F, Kreuger R, et al. VECTOR: a preclinical imaging system for simultaneous submillimeter SPECT and PET. *J Nucl Med* 2013;54(2):306–12.
- [22] van der Have F, Vastenhout B, Ramakers RM, et al. U-SPECT-II: An Ultra-High-Resolution Device for Molecular Small-Animal Imaging. *J Nucl Med* 2009;50(4):599–605.
- [23] Branderhorst W, Vastenhout B, van der Have F, et al. Targeted multi-pinhole SPECT. *Eur J Nucl Med Mol Imaging* 2011;38(3):552–61.
- [24] Vaissier PEB, Goorden MC, Vastenhout B, et al. Fast spiral SPECT with stationary γ -cameras and focusing pinholes. *J Nucl Med* 2012;53(8):1292–9.
- [25] Branderhorst W, Vastenhout B, Beekman FJ. Pixel-based subsets for rapid multi-pinhole SPECT reconstruction. *Phys Med Biol* 2010;55(7):2023–34.
- [26] van der Have F, Vastenhout B, Rentmeester M, Beekman FJ. System calibration and statistical image reconstruction for ultra-high resolution stationary pinhole SPECT. *IEEE Trans Med Imaging* 2008;27(7):960–71.
- [27] Goorden MC, van der Have F, Kreuger R, Beekman FJ. An efficient simulator for pinhole imaging of PET isotopes. *Phys Med Biol* 2011;56(6):1617–34.
- [28] Goorden MC, van der Have F, Beekman FJ. Optimizing image reconstruction for simultaneous sub-mm clustered pinhole PET-SPECT. *Proceeding of the 12th Fully 3D Meeting* 126–129; 2013.
- [29] King MA, Glick SJ, Pretorius PH, et al. Wernick MN. Attenuation, scatter, and spatial resolution compensation in SPECT. *Emission Tomography: The Fundamentals of PET and SPECT*. London: Elsevier Academic; 2004. p. 473–98.
- [30] Wu C, de Jong JR, Gratama van Andel HA, et al. Quantitative multi-pinhole small-animal SPECT: uniform versus non-uniform Chang attenuation correction. *Phys Med Biol* 2011;56:N183–93.
- [31] Treuting PM, Dintzis SM. Comparative anatomy and histology a mouse and a human atlas. Amsterdam: Elsevier; 2012 211–28.
- [32] Dou S, Smith M, Wang Y, Ruszkowski M, Liu G. Intraperitoneal injection in not always a suitable alternative to intravenous injection for radiotherapy. *Cancer Biother Radiopharm* 2013;28(3):335–42.
- [33] Zuckier LS, Li Y, Chang CJ. Evaluation in a Mouse Model of a Thyroid-blocking Protocol for 131I Antibody Therapy (Short Communication). *Cancer Biother Radiopharm* 1998;13(6):457–60.
- [34] Brandt MP, Kloos RT, Shen DH, et al. Micro-Single-Photon Emission Computer Tomography Image Acquisition and Quantification of Sodium-Iodide Symporter-Mediated Radionuclide Accumulation in Mouse Thyroid and Salivary Glands. *Thyroid* 2012;22(6):617–24.
- [35] Zuckier LS, Dohan O, Li Y, et al. Kinetics of Perrhenate Uptake and Comparative Biodistribution of Perrhenate, Pertechnetate, and Iodine by Nal Symporter-Expressing Tissues In Vivo. *J Nucl Med* 2004;45(3):500–7.
- [36] Hwang AB, Franc BL, Gulberg GT, Hasegawa BH. Assessment of the sources of error affecting the quantitative accuracy of SPECT imaging in small animals. *Phys Med Biol* 2008;53:2233–52.
- [37] Sgouros G, Kolbert KS, Sheikh A, et al. Patient-Specific Dosimetry for ¹³¹I Thyroid Cancer Therapy Using ¹²⁴I PET and 3-Dimensional-Internal Dosimetry (3D-ID) Software. *J Nucl Med* 2004;45(8):1366–72.
- [38] McFarlane AS. Labelling of plasma proteins with radioactive iodine. *Biochem J* 1956;62(1):135–43.
- [39] Franken PR, Guglielmi J, Vanhove C, et al. Distribution and Dynamics of ^{99m}Tc-Pertechnetate Uptake in the Thyroid and Other Organs Assessed by Single-Photon Emission Computed Tomography in Living Mice. *Thyroid* 2010;20(5):519–26.